ACS APPLIED MATERIALS & INTERFACES

www.acsami.org

Research Article

Facile Synthesis of Electrically Conductive and Heatable Nanoparticle/Nanocarbon Hybrid Aerogels

Dong Xia,* Jamie Mannering, Qun Li, Alexander F. Massey, Alexander N. Kulak, Heng Li,* Robert Menzel, and Peng Huang*

Cite This: *ACS Appl. Mater. Interfaces* 2021, 13, 36201−36212

Read Online

ACCESS | Metrics & More | Article Recommendations | Supporting Information

ABSTRACT: Joule heating studies on nanoparticle/nanocarbon hybrid aerogels have been reported, but systematic investigations on hydrotalcite-derived catalysts supported onto reduced graphene oxide (rGO) aerogels are rare. In this study, hydrotalcite-derived Cu-Al_2O_3 nanoparticles were incorporated into a porous and multifunctional rGO aerogel support for fabricating electrically conducting Cu-Al_2O_3/rGO hybrid aerogels, and their properties were investigated in detail. The hybridization of Cu-Al_2O_3 with a 3D nanocarbon support network imparts additional functionalities to the widely used functional inorganic nanoparticles, such as direct electrical framework heating and easy regeneration and separation of spent nanoparticles, with well-spaced nanoparticle segregation. 3D variable-range hopping model fitting confirmed that electrons were able to reach the entire aerogel to enable uniform resistive heating. The conductivity of the nanocarbon support framework facilitates uniform and fast heating (up to 636 K/min) of the embedded nanoparticles at very low energy consumption, while the large porosity and high thermal conductivity enable efficient heat dissipation during natural cooling (up to 336 K/min). The thermal stability of the hybrid aerogel was demonstrated by repeated heating/cooling cycling at different temperatures that were relevant to important industrial applications. The facile synthetic approach can be easily adapted to fabricate other types of multifunctional nanoparticle/nanocarbon hybrid aerogels, such as the MgAl-MMO/rGO aerogel and the Ni-Al_2O_3/rGO aerogel. These findings open up new routes to the functionalization of inorganic nanoparticles and extend their application ranges that involve electrical/thermal heating, temperature-dependent catalysis, sorption, and sensing.

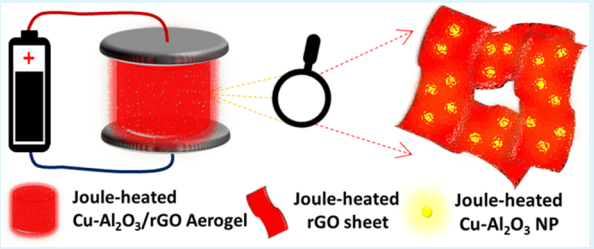

KEYWORDS: *graphene aerogel, nanoparticle/nanocarbon hybrid, Joule heating, support framework, layered double hydroxide, inorganic nanoparticles*

INTRODUCTION

Layered double hydroxides (LDHs) or hydrotalcites (HTs) are lamellar structured materials that are composed of positively charged layers and negatively charged anions that are embedded in the interlayers.[1−3] These types of materials have been widely exploited in various applications, owing to the versatility of their chemical compositions and their physical−chemical properties.[4] The general formula of LDHs takes the form of $[M_{1-x}^{2+}M_x^{3+}(OH)_2]^{x+}(A^{n-})_{x/n}\cdot mH_2O$. Here, M^{2+}/M^{3+} represents the divalent/trivalent metal cations and A^{n-} represents the anions. By replacing the metal cations in the lattice structure, the application range of LDH-derived materials has been extended to various fields, including catalysis (CuAl-LDH, CoAl-LDH),[5,6] supercapacitors (NiAl-LDH, NiCo-LDH),[7,8] and water splitting (NiFe-LDH, CoMn-LDH).[9,10] Alternatively, the performance of the materials can be enhanced by substituting the intercalated anions through an ion exchange process. Taking advantage of the expandable lamellar structure, these nanosheets can be assembled into a wide range of hierarchically structured hybrid materials and polymer nanocomposites.

LDHs have also been used as the precursor in the syntheses of multifunctional mixed metal oxides (MMOs).[1] These processes involve the calcination or thermal reduction of nanoparticles, which consequently affect the metal electronic configuration, surface area, particle size, morphology, and reducibility. Among these MMOs, Cu-Al_2O_3 nanoparticles, fabricated by solvent-deficient precipitation methods, have gained great attention in catalytic hydrogenation applications.[11−13] For instance, the octanal conversion efficiency of up to 99% from a mixture of octanal and octene using the Cu-Al_2O_3 catalyst has been achieved because the unpaired electrons in the *d*-band of copper adsorb hydrogen to promote catalytic efficiency.[11] So far, very few studies have attempted the synthesis of Cu-Al_2O_3 nanoparticles from the CuAl-LDH

Received: June 4, 2021
Accepted: July 13, 2021
Published: July 22, 2021

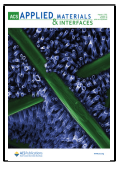

precursor. Many catalytic reactions were shown to be temperature-dependent and were typically heated with the aid of external, low-efficient, and high energy-demanding radiative heat transfer processes. To improve the efficiency of the catalytic process, it is advantageous to provide the Cu-Al_2O_3 nanoparticles with the direct electrical heating ability and the ability to switch to the desired temperatures quickly, with minimal energy consumption.

Nanocarbon aerogels have exhibited promising features as 3D stabilizing support frameworks for various types of inorganic functional nanoparticles in the fabrication of nanoparticle/nanocarbon hybrids. One of the more interesting characteristics of nanocarbon aerogels is their ability to be directly heated by applying an electrical current (Joule heating). When combined with the functional nanoparticles, the interconnected graphitic microstructure of the conductive support framework allows uniform local electrical resistive heating that covers the entire hybrid aerogel structure, leading to more homogeneous, faster, and energy-efficient heating, compared to the traditional radiative heating process. The formation of robust and hierarchical microchannels in the hybrid aerogels offers advantages of large surface areas, diverse porosities, outstanding mechanical properties, excellent thermal conductivities, and efficient material recycling.[14] On the other hand, the nanocarbon support framework also effectively inhibits nanoparticle aggregation during material fabrication, thus helping in exposing more effective reaction sites. In this study, CuAl-LDH was used as the precursor for the synthesis of Cu-Al_2O_3 nanoparticles and was embedded into a 3D rGO aerogel support framework in the preparation of multifunctional porous hybrid materials that exhibit enhanced performance and unique features of energy-efficient, direct local resistive heating. Our previous work[1] has demonstrated the feasibility of fabricating electrically conductive nanoparticle/nanocarbon hybrid aerogels for adsorptive applications. Here, we further extended the current application range by introducing industrially important inorganic catalysts into the hybrid aerogels. In addition to the thorough investigation of the structure and electrothermal properties of the hybrid aerogel, we also looked into the mechanical performance and charge transport mechanism, and discussed the roles of the additives in the fabrication of the aerogel to provide a more comprehensive characterization and in-depth understanding of the material. A universal synthetic approach to the in situ fabrication of other types of inorganic nanoparticles, supported onto the rGO aerogel (e.g., MgAl-MMO/rGO aerogel and Ni-Al_2O_3/rGO aerogel), is also demonstrated. The differences between the unsupported nanoparticles and the nanocarbon-supported hybrid aerogels were compared.

MATERIALS AND METHODS

Materials. Graphene oxide (GO) was purchased from William Blythe Limited (U.K.). $Cu(NO_3)_2{\cdot}3H_2O$ (99%), $Mg(NO_3)_2{\cdot}6H_2O$ (99%), $Ni(NO_3)_2{\cdot}6H_2O$ (99%), $Al(NO_3)_3{\cdot}9H_2O$ (98%), sucrose, and poly(vinyl alcohol) (PVA) were obtained from Sigma-Aldrich (U.K.). Toluene, NaOH, Na_2CO_3, and HPLC water were supplied by Fisher Scientific (U.K.). All chemicals were used as received.

Synthesis of Cu-Al_2O_3 Nanoparticles. An aqueous solution consisting of 24 mL of 0.67 M $Cu(NO_3)_2$ and 0.33 M $Al(NO_3)_3$ were added at a constant speed to an aqueous alkaline reservoir (100 mL, 0.01 M NaOH, pH 12) at 50 °C, using a peristaltic pump. The pH of the mixture was constantly monitored with a pH probe and adjusted to 10 by slow addition of base solutions (1 M NaOH, 1 M Na_2CO_3), using a second peristaltic pump. Once completed, the synthesized blue suspension was aged at 50 °C for 20 h. Finally, the resultant suspension was centrifuged and the solid was washed with HPLC water until the pH value of the supernatant reached 7. Wet CuAl-LDH pastes were immediately used for aerogel fabrication to minimize nanoparticle aggregation. To obtain the Cu-Al_2O_3 powder samples, the synthesized blue precipitate was oven-dried at 50 °C to a constant weight, and then thermally reduced in a tube furnace (Carbolite Gero, U.K.) at 1000 °C under a H_2/N_2 atmosphere (5% H_2) for 2 h.

Synthesis of Cu-Al_2O_3/rGO Hybrid Aerogels. PVA and sucrose (0.42 g, weight ratio 1:1) were dissolved in 55 mL of HPLC water and mixed with 0.42 g of GO flakes, using a tip sonicator, to which, half of the previously obtained CuAl-LDH wet paste was added, followed by tip sonication to give a sufficiently mixed CuAl-LDH wet paste and GO/polymer suspension. Then, 13.5 mL toluene was added and the mixture was stirred vigorously for 5 min. A small amount of the mixture (3.5 mL) was transferred into a customized, cylindrical poly(ether-ether-ketone) (PEEK) mold with a matching copper cap. Finally, the mixture-filled mold was immersed in liquid nitrogen for 10 min and then freeze-dried overnight to yield the CuAl-LDH/GO aerogel. An electrically conducting Cu-Al_2O_3/rGO aerogel (diameter × height = ∼1.5 cm × ∼1.3 cm) was obtained by thermally reducing the CuAl-LDH/GO aerogel following the same thermal reduction procedure. For comparison, a CuAl-LDH/GO aerogel and Cu-Al_2O_3/rGO aerogel with no addition of the polymer and toluene were also synthesized. Detailed procedures for the synthesis of the MgAl-MMO powder, MgAl-MMO/rGO aerogel, Ni-Al_2O_3 powder, and Ni-Al_2O_3/rGO aerogel are described in the Supporting Information.

Joule Heating Measurements. Joule heating studies of the Cu-Al_2O_3/rGO aerogels were conducted, using a designed Joule heating setup, under a nitrogen atmosphere (Figure S1, ESI). The as-prepared Cu-Al_2O_3/rGO aerogel was attached tightly between the electrodes. Then a thermocouple with a temperature data logger was inserted into the center of the aerogel to record the core temperature. The surface temperature of the aerogel was recorded simultaneously using another thermocouple. The Joule heating pre-conditioning of the Cu-Al_2O_3/rGO aerogel was performed at a core temperature of 100 °C for 20 min to remove any volatiles (e.g., water and gases, Figure S2, ESI). This step is essential if one is to obtain a stable and repeatable Joule heating performance. The Joule heating temperature was controlled via the tuning of the electrical current provided by the power supply (Figure S3, ESI). The thermal conductivity of each aerogel was measured according to a reported temperature gradient fitting method.[15] The corresponding temperature, voltage, and current variations were recorded by data loggers.

Materials Characterization. X-ray diffraction (XRD) of the specimens was performed on a Bruker D2 Phaser diffractometer using Cu Kα radiation, with a step size of θ = 0.01013°. The crystallite domain sizes were calculated using the Scherrer equation and Bragg's law was used to calculate the lattice spacings. Brunauer–Emmett–Teller (BET) surface area measurements were performed using a Micromeritics TriStar 3000 instrument. The samples were degassed in N_2 at 110 °C for 3 h before analysis and N_2 adsorption and desorption isotherms were measured at 77 K. The Barrett–Joyner–Halenda (BJH) method was used to determine the pore size distribution of the samples by calculation of the desorption isotherm. Raman spectroscopic analyses were conducted using a Renishaw InVia Raman microscope with an excitation laser wavelength of 532 nm, between 400 and 4000 cm^{-1}. Cu K-edge X-ray absorption near edge structure (XANES) measurements were carried out on beamline B18 at Diamond Light Source (Oxfordshire, U.K.). The samples were deposited onto double-sided adhesive carbon tape and then mounted onto the aluminum sample holders. X-ray photoelectron spectroscopic (XPS) analysis was conducted using Thermo Fisher Scientific K-Alpha$^+$ equipment; the high-resolution scans were obtained at a pass energy of 30 eV and a step size of 0.1 eV. The binding energies were referenced to the C 1s peak of adventitious carbon at 284.8 eV. Scanning electron microscopic (SEM) analyses were performed on a Nova NanoSEM 450 with an accelerating voltage of 3 keV. The specimens were fixed onto aluminum stubs using conductive carbon

https://doi.org/10.1021/acsami.1c10428
ACS Appl. Mater. Interfaces 2021, 13, 36201–36212

tape. Energy-dispersive X-ray (EDX) spectroscopic analysis was conducted on the same SEM instrument at an accelerating voltage of 18 keV. Transmission electron microscopic (TEM) analyses of the specimens were performed on an FEI Tecnai F30 high-resolution analytical transmission electron microscope, at an accelerating voltage of 300 keV. The samples were dispersed in ethanol, cast onto a copper grid, and dried before analysis. Thermogravimetric analyses (TGA) were conducted on a PerkinElmer Pyris One instrument, under an air atmosphere. The samples were heated from ambient temperature to 950 °C, at a heating rate of 10 °C·min^{-1}. The compressive strength tests were conducted using an Instron 5566 universal testing machine, at a loading speed of 1 mm/min. Thermal images were taken using a thermal camera (Fluke TiR1) and analyzed using Fluke Connect software.

RESULTS AND DISCUSSION

Materials Syntheses and Characterization. Details of the fabrication of the Cu-Al_2O_3/rGO hybrid aerogels and the subsequent Joule heating measurements are illustrated in ESI Figure S4, for which the 3D cylindrical, monolithic aerogel was attached between macroscopic electrodes for resistive local framework heating. The successful preparation of non-thermally reduced CuAl-LDH powder was verified by the characteristic peaks of hydrotalcite for the basal planes of (003), (006), (100), (012), (015), (107), (108), and (110) (Figure 1a), consistent with reported results.[16] XRD analysis confirmed the formation of metallic copper particles in both the Cu-Al_2O_3 powder and the Cu-Al_2O_3/rGO aerogel (Figure 1a). Three pronounced characteristic peaks emerged at 43.2, 50.3, and 74.0°, which were derived from the (111), (200), and (220) planes of the metallic copper particles, in line with the reported studies.[17] No diffraction peak relating to Al_2O_3 appeared in the XRD pattern, because of its highly amorphous structure.[1] The broad characteristic peak at 26.2° for the Cu-Al_2O_3/rGO aerogel, Figure 1b, originated from the (002) plane of the rGO sheets,[18] suggesting that the Cu-Al_2O_3 nanoparticles and the rGO sheets were well-combined in the 3D monolithic aerogel. All of the characteristic peaks for the Cu-Al_2O_3/rGO aerogel were much broader than those of the Cu-Al_2O_3 powder, likely indicating the formation of smaller copper particles in the hybrid aerogel.

To verify this observation, the lattice spacing ($d_{spacing}$, nm) and the average crystallite domain size (D_p, nm) of the samples were calculated from the XRD diffraction peaks, using the Scherrer equation (Table 1). The identical $d_{spacing}$ value for the powder and the hybrid aerogel implies that the introduction of the rGO support had no significant impact on the particle lattice structure. The Cu-Al_2O_3 powder exhibited an average crystallite domain size, D_p, of 41.5 nm, whereas the D_p value of the hybrid aerogel decreased by 65% to only 14.5 nm (Table 1). This confirms that the rGO sheets effectively inhibited nanoparticle aggregation during the thermal reduction treatments. When dividing the (002) crystallite domain size, D_{002} (i.e., the crystallite size in the direction of the rGO sheets stacking), by the basal plane spacing of the rGO sheet, d_{002}, the number of rGO sheets in the crystallite domain, i.e., the average number of sheets stacked with high crystalline order, can be estimated. Scherrer analysis indicates that the hybrid aerogel possessed 5 layers of rGO sheets along the (002) direction of the crystallites. When oxidized under an air atmosphere, the weight of the Cu-Al_2O_3 powder increased by 20% before reaching equilibrium, due to the transformation of metallic copper to copper oxide. For the Cu-Al_2O_3/rGO aerogel, TGA, and the derivative TGA curves clearly showed

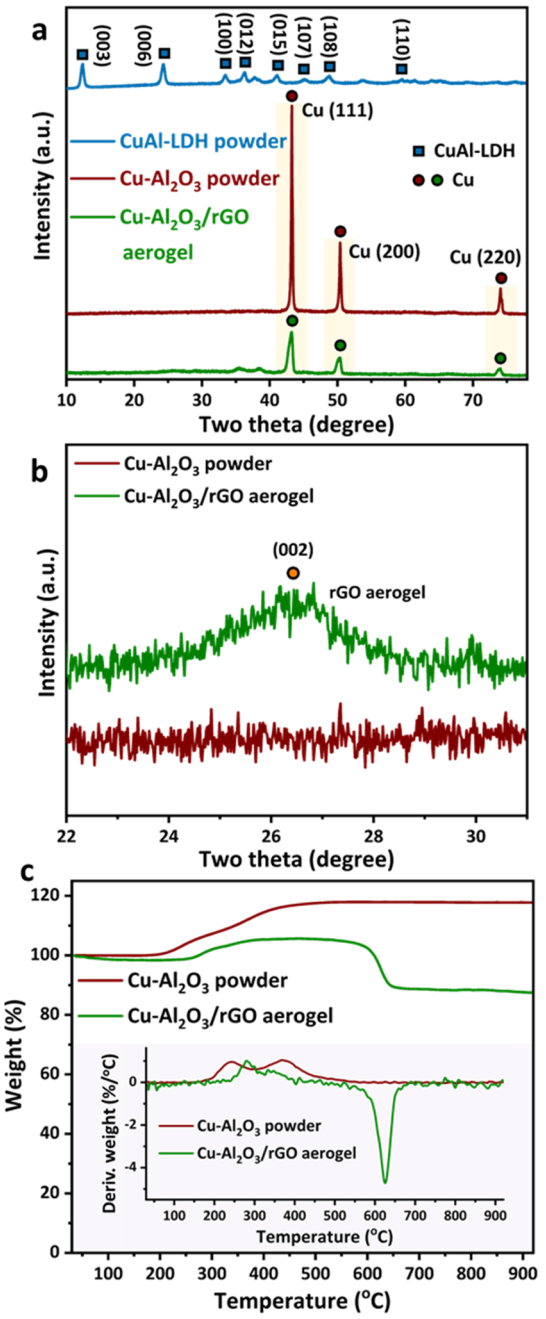

Figure 1. (a, b) XRD patterns and (c) TGA curves of Cu-Al_2O_3 powder and Cu-Al_2O_3/rGO aerogel (inset: DTG curves).

an additional weight loss at around 550 °C, which was attributed to the combustion of the rGO aerogel (Figure 1c). From the results obtained from the TGA curves and EDX analysis, the weight percentages of Cu and Al_2O_3 in the hybrid aerogel were calculated to be 53.9 and 20.4%, respectively.

BET surface area analysis of the Cu-Al_2O_3 powder and the Cu-Al_2O_3/rGO aerogel both exhibited typical type-IV isotherms (Figure 2a), suggesting the existence of a copious mesoporous structure. This was further confirmed by BJH pore diameter distribution analyses, as shown in Figure 2b. Both the powder and the aerogel showed a large number of mesopores at ~43 nm. A narrower mesopore size distribution caused by the introduction of interconnected rGO sheets in the hybrid aerogel is beneficial for exposing more active sites for sorption

https://doi.org/10.1021/acsami.1c10428
ACS Appl. Mater. Interfaces 2021, 13, 36201−36212

Table 1. Physical Properties of Cu-Al_2O_3 Powder and Cu-Al_2O_3/rGO Aerogel

materials	D_p (nm)[a]	$d_{spacing}$ (nm)[b]	SSA (m^2/g)[c]	V_{pore} (cm^3/g)[d]	mesopore size (nm)[e]	σ (S/m)[f]
Cu-Al_2O_3 powder	41.5	0.20	23	0.14	48	0
Cu-Al_2O_3/rGO aerogel	14.5	0.20	66	0.21	38	3.9

[a]D_p, average crystallite domain size, as calculated from the (111) plane. [b]$d_{spacing}$, lattice spacing. [c]SSA, specific surface area, as obtained from BET measurements. [d]V_{pore}, accumulative pore volume, as derived from BET measurements. [e]Average mesopore diameters, as derived from the BJH mesopore size distributions. [f]σ, electrical conductivity.

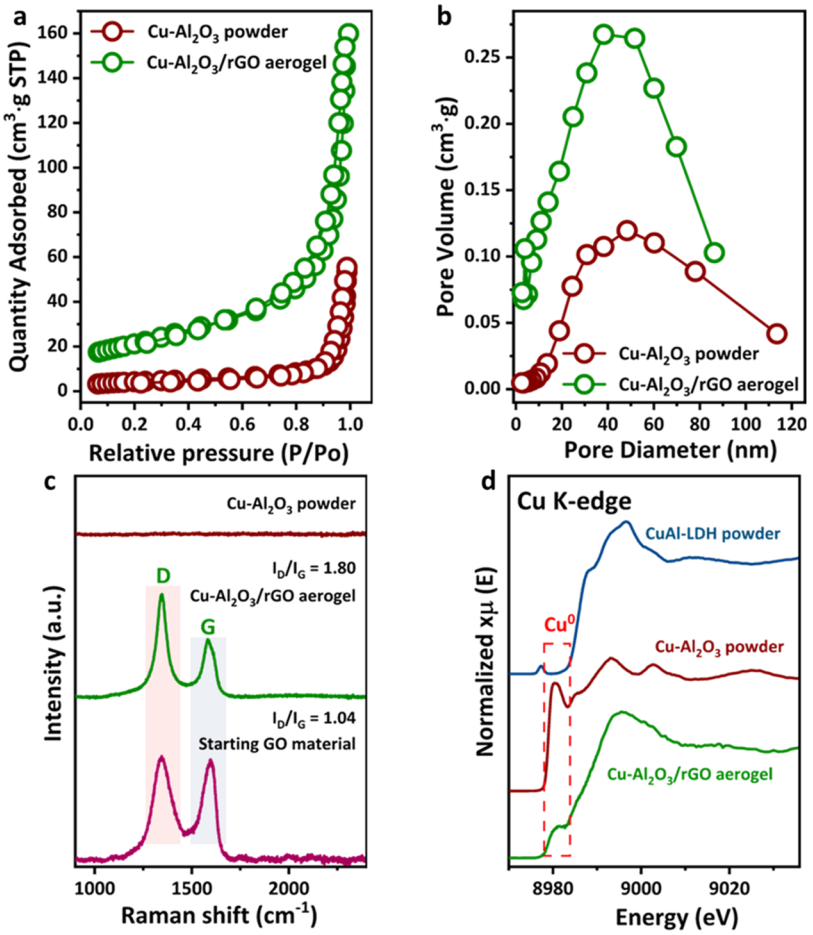

Figure 2. (a, b) N_2 sorption isotherms and BJH diameter distributions of the Cu-Al_2O_3 powder and Cu-Al_2O_3/rGO aerogel. (c) Raman spectra of GO, Cu-Al_2O_3 powder, and Cu-Al_2O_3/rGO aerogel. (d) Cu K-edge XANES spectra.

and catalytic applications.[1] As expected, the hybrid aerogel showed an almost three times larger specific surface area (SSA, 66 m^2/g) than the unsupported Cu-Al_2O_3 powder (23 m^2/g), coupled with a 50% increase in the pore volume accumulations (Table 1). These enhancements are exclusively derived from the effective separation and good distribution of the nanoparticles by the rGO sheets and the polymer-derived carbon products acting as the support frameworks in the hybrid structure. A significant increase in the graphiticity of the GO support framework was observed in Raman spectroscopic analysis, as indicated by a 73% increase of the I_D/I_G ratio from 1.04 to 1.80 (Figure 2c); consistent with reported Raman results of thermally reduced GO.[1] The increased graphiticity was attributed to the presence of polymer-derived carbon products and high-temperature reduction induced restoration of the graphitic structure during the fabrication of the hybrid aerogel (Figure S5, ESI). The normalized Cu K-edge XANES spectra showed the characteristic absorption edge and the peak of elemental Cu, further confirming the reduction of the Cu^{2+} species to the Cu^0 state in both Cu-Al_2O_3 powder and the hybrid aerogel (Figure 2d and the first derivative curves in Figure S6, ESI).[19] The XPS survey scans demonstrated the existence of only carbon, oxygen, copper, and aluminum atoms in the as-prepared materials (Figure S7, ESI). Deconvolution of the XPS high-resolution spectra in the Al 2p region confirmed that all of the aluminum species in CuAl-LDH were transformed into aluminum oxide,[1] which acted as additional supports for the copper species (Figure S8, ESI).

The digital image of the Cu-Al_2O_3 powder (Figure 3a) provided direct visual evidence for the generation of metallic copper in the powder, while Figure 3d shows an intact monolithic, 3D bulk of the Cu-Al_2O_3/rGO aerogel, highlighting the distinctive morphologies between the two types of material. SEM micrographs of the Cu-Al_2O_3 powder showed large and highly aggregated particles, arising from high-temperature sintering (Figure 3b,c), consistent with the low BET specific surface area results. In direct contrast, SEM micrographs of the Cu-Al_2O_3/rGO aerogel exhibited highly

https://doi.org/10.1021/acsami.1c10428
ACS Appl. Mater. Interfaces 2021, 13, 36201−36212

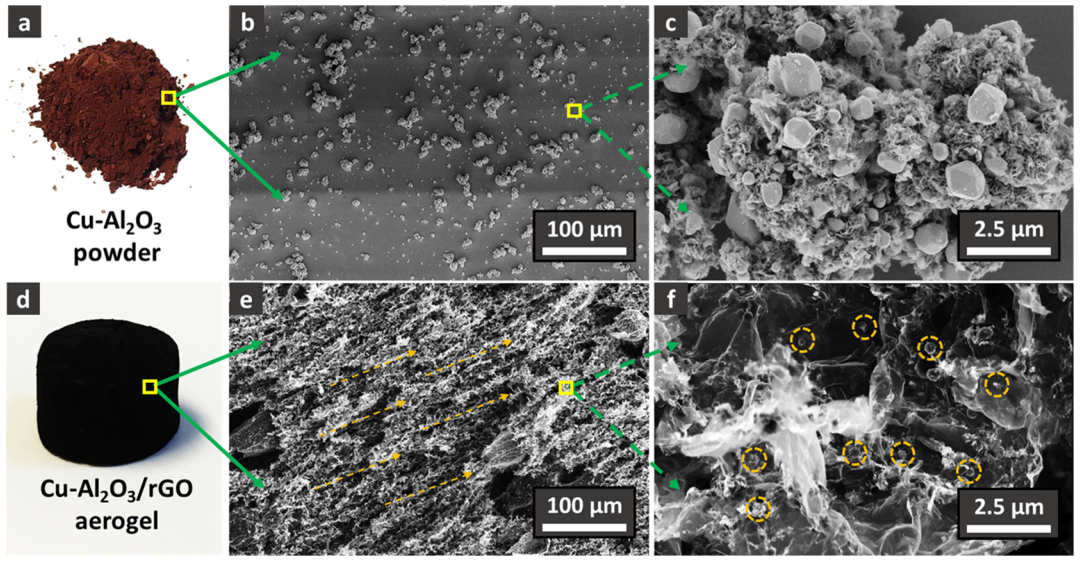

Figure 3. (a) Digital image of the Cu-Al_2O_3 powder. (b, c) SEM micrographs of the Cu-Al_2O_3 powder at different magnifications. (d) Digital image of the Cu-Al_2O_3/rGO aerogel. (e, f) SEM micrographs of the Cu-Al_2O_3/rGO aerogel at different magnifications.

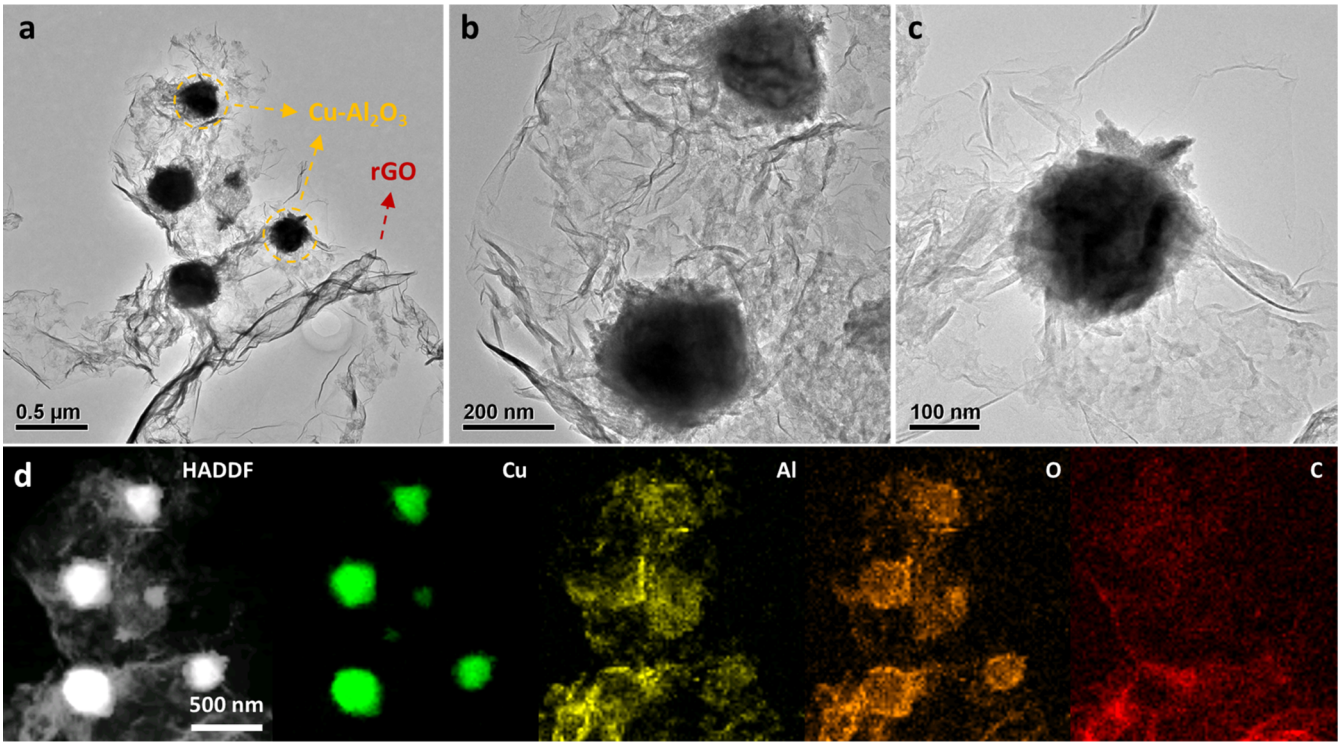

Figure 4. (a–c) TEM micrographs of the Cu-Al_2O_3/rGO aerogel at different magnifications. (d) TEM-EDX mapping of the selected areas for the analysis of Cu, Al, O, and C elements.

aligned channels and various porous microstructures,[20,21] formed by the rGO sheets, which were caused by the unidirectional growth of ice crystals during fabrication (Figure 3e and ESI Figure S9).[22] High-resolution SEM micrographs of the hybrid aerogel demonstrated that the Cu-Al_2O_3 nanoparticles were well-dispersed and tightly anchored on the surface of the rGO sheets (Figure 3f), further corroborating the effectiveness of the rGO nanostructure as an excellent support framework for inhibiting nanoparticle aggregation. It is worth noting that the non-reduced CuAl-LDH/GO aerogel precursors exhibited distinct internal microstructures and morphologies compared to the reduced form of the hybrid aerogel (Figures S10 and S11, ESI).

SEM-EDX analysis implied that the hybrid aerogel was composed of only C, O, Cu, and Al atoms (Figure S12, ESI), consistent with the XPS survey scan result (Figure S7, ESI). The atomic percentages of Cu and Al were 21.6 and 10.2%, respectively, very close to the added nominal Cu/Al molar ratio of 2:1. The uniform Cu-Al_2O_3 particle distribution was confirmed by the SEM-EDX mapping of the aerogel "flake" surface at different magnifications (Figure S12, ESI). TEM micrographs further confirmed that the Cu-Al_2O_3 nano-

https://doi.org/10.1021/acsami.1c10428
ACS Appl. Mater. Interfaces 2021, 13, 36201−36212

particles were well-spaced and attached tightly to the surface of the rGO sheets (Figure 4a–c). TEM-EDX mapping (Figure 4d) not only demonstrated the uniform distribution of Cu, Al, O, and C elements in the hybrid aerogel (in line with the SEM-EDX mapping, Figure S12, ESI) but also indicated the functionality of Al_2O_3 as the support for the metallic Cu nanoparticles (consistent with the XPS analyses, Figure S8, ESI).

Joule Heating Characteristics of the Cu-Al_2O_3/rGO Aerogel. The Cu-Al_2O_3/rGO aerogel showed relatively high compressive yield strength (stress of 34 kPa and strain of 16%). These characteristics are crucial prerequisites for the aerogel to be used for Joule heating studies under electrode compression (less than 7% strain) while maintaining its structural integrity (Figure S13, ESI). Considering its excellent properties and relatively high compressive strength,[23] the Cu-Al_2O_3/rGO aerogel was used in an investigation of the electrical characteristics and the thermal characteristics, using a custom-made Joule heating setup, as shown in Figure 5a. The mechanical robustness of the Cu-Al_2O_3/rGO aerogel was attributed to the physical and covalent crosslinking of the rGO framework. Physical crosslinking was derived from the graphitization of the original GO during the annealing treatment process, under high-temperature and reducing conditions, which led to significantly increased van der Waals interactions among the rGO framework components. Covalent crosslinking was achieved through the thermal decomposition of the PVA and sucrose additives in the original GO aerogels. This process resulted in the formation of graphitized high-molecular-weight components that covalently crosslink the rGO sheets in the aerogel framework.[15,24] PVA and sucrose acted as binders which help maintain the structure and shape of the aerogel after lyophilization and also during the subsequent annealing treatment. On the other hand, the decomposition of the additives during high-temperature annealing gave rise to a "liquid-phase sintering" type process that effectively strengths the final hybrid aerogel.[24] After pre-conditioning (i.e., removal of adsorbed water and gases), the hybrid aerogel exhibited a very good linear correlation between the Joule heating-induced temperature and the power density (R^2> 0.998, Figure 5b), indicating excellent electrothermal stabilities at temperatures of up to 400 °C and the relative ease of precise Joule heating-temperature-control via tuning the power input. A decrease in the resistivity of the hybrid aerogel was attributed to the semiconducting behavior of defective carbon nanomaterials.[1] The electrical conductivity (σ) of the hybrid aerogel increased slightly with the increase in the temperature (ranging from 3.9 to 5.8 S/m), owing to more free carriers moving at a higher temperature (Figure 5c). The σ values of the hybrid aerogel were smaller than those of the reported pure rGO aerogel,[15] because of the extensive impregnation of the segregated inorganic powder. A constant thermal conductivity (κ) within the investigated temperature range suggested that only normal-process phonon–phonon scattering exists in the aerogel during heat dissipation (Figure 5c).[25]

To assess the charge transport mechanism within the conducting network, a 3D variable-range hopping (VRH) model was applied to the acquired data. This takes the form of $\sigma(T) = \sigma_0 \cdot T^{-1/2} \cdot \exp(-(T_0/T)^{1/4})$, where σ represents the aerogel electrical conductivity (S/m); σ_0 is the electrical conductivity prefactor; and T_0 and T are the temperature coefficient and the Joule heating temperature, respectively.[26]

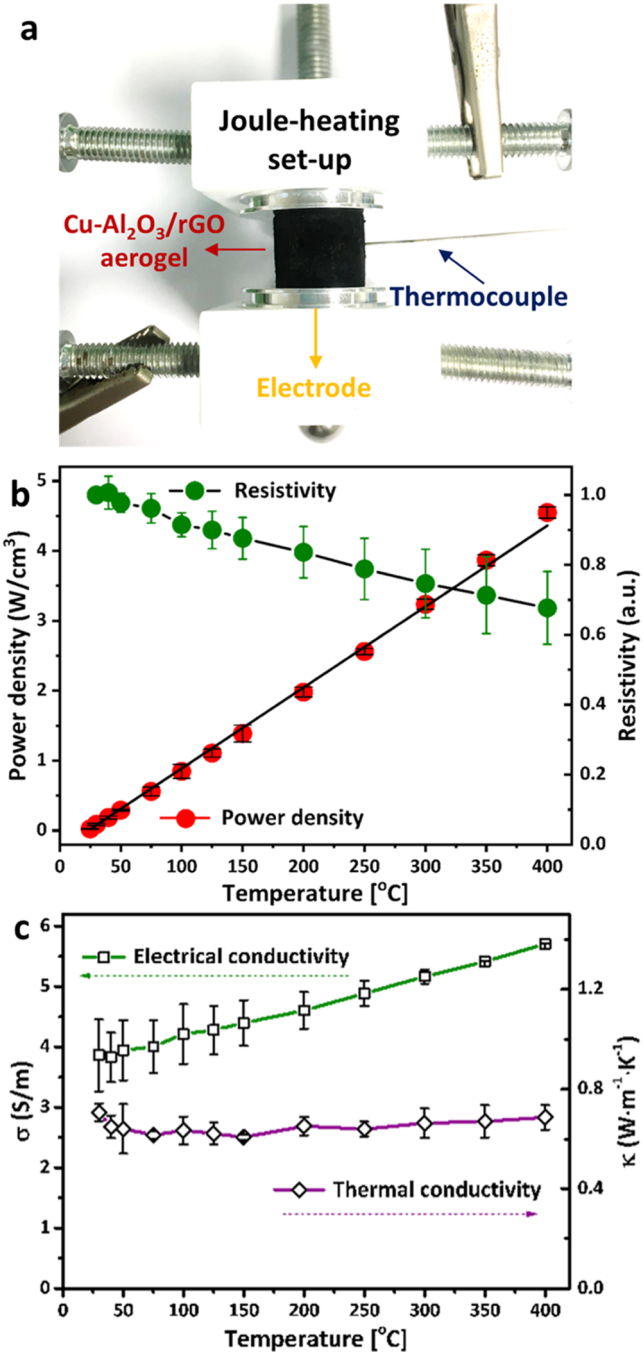

Figure 5. (a) Digital image of a Cu-Al_2O_3/rGO aerogel embedded in the custom-made Joule heating setup. (b) Power density and resistivity versus Joule heating temperature (c) Electrical/thermal conductivities versus Joule heating temperature of the Cu-Al_2O_3/rGO aerogel.

The excellent fit (R^2 > 0.996, Figure 6a) confirmed the dominant carrier transport mechanism to be 3D variable-range hopping, the hopping electrons were able to reach the entire aerogel to enable uniform resistive heating.[26] The Arrhenius thermal activation model was utilized to calculate the bandgap value of the Cu-Al_2O_3/rGO aerogel, as expressed by $\sigma(T) = \sigma_a \cdot \exp(-E_a/k_B \cdot T)$, where σ_a is a pre-exponential factor; E_a is the activation energy (eV, also bandgap here); and k_B is the Boltzmann's constant.[26] The very small value of E_a (0.017 eV, Figure 6b) implied excellent electrical conductivity of the

https://doi.org/10.1021/acsami.1c10428
ACS Appl. Mater. Interfaces 2021, 13, 36201–36212

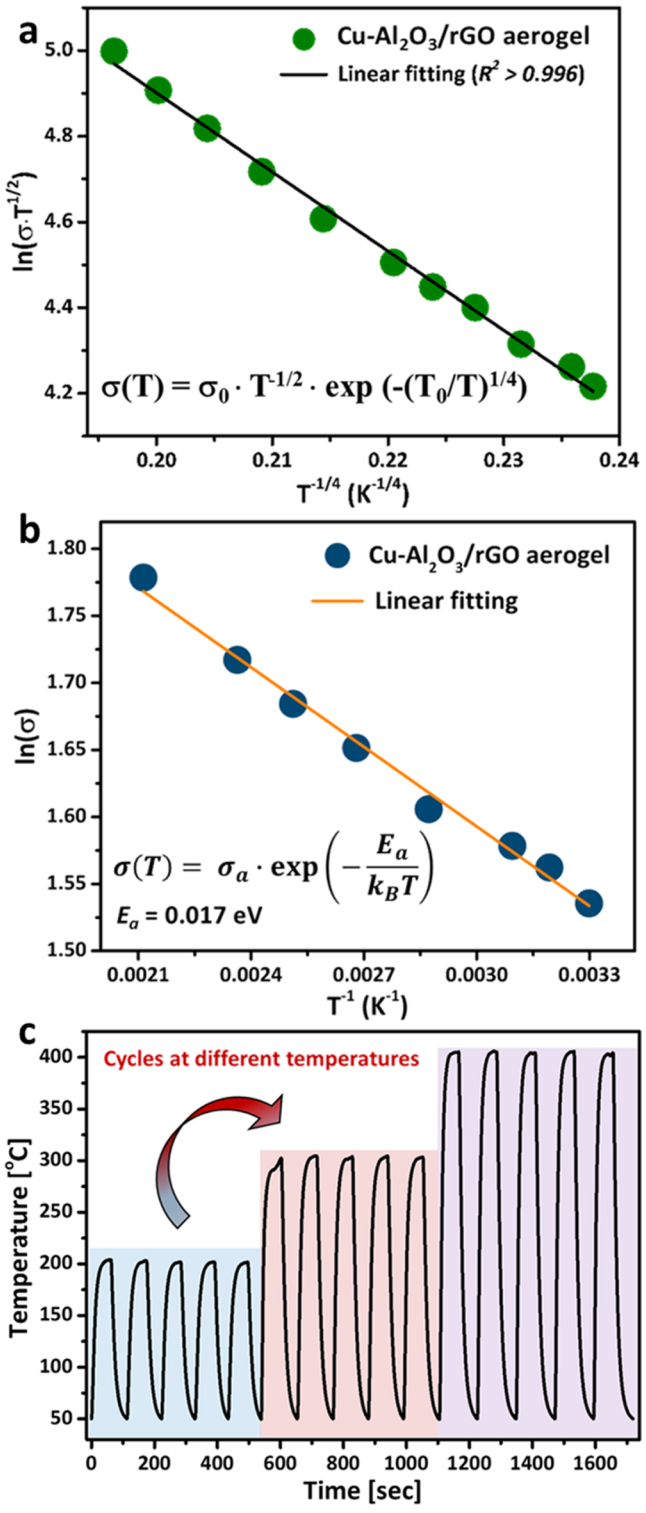

Figure 6. (a) Fit of the 3D VRH model, $\ln(\sigma \cdot T^{1/2})$ versus $T^{-1/4}$. (b) Fit of the Arrhenius thermal activation model, $\ln(\sigma)$ versus T^{-1}. (c) Cycling performance of the aerogel at different Joule heating temperatures.

hybrid aerogel. This observation is supported by the stable and repeatable heating/cooling cycling performance of the hybrid aerogel at various temperatures (200−400 °C, Figure 6c and ESI Figure S14a), pertinent to practical applications.

Interestingly, the heating rate almost tripled (210−636 K/min) when the Joule heating temperature increased from 200 to 400 °C, although the cooling rate increased only by 56% (Figure S14b,c, ESI). The highly efficient heating can be mainly attributed to the local nature of the resistive framework heating process, a prominent feature that is not achievable when using a relatively slow external heating process via radiative heat transfer (Figure S15, ESI). The large porosity and high thermal conductivity of the support framework allow efficient heat dissipation when the power supply is switched off. The fast heating/cooling kinetics enables efficient temperature-swing cycling of the embedded nanoparticles. These have great potential for exploitation in fields of catalytic processes or energy-efficient exhausted adsorbent regeneration. These findings highlight the advantages of deploying energy-efficient and direct local resistive framework heating for embedded functional nanoparticles, offering fast thermal cycling kinetics, as well as convenient and precise temperature control, at significantly reduced energy consumption. Compare with the other reported 3D conductive composites,[27−29] the Cu-Al_2O_3/rGO hybrid aerogel in this study excels in both electrical and thermal conductivity performances.

The highly effective syntheses employed in this study can be easily adapted for the introduction of other types of functional nanoparticles onto the nanocarbon support framework, thus significantly extending the current application range towards sorption, electro-catalysis, etc. MgAl-mixed metal oxides (MgAl-MMO) and Ni-Al_2O_3 hybrid aerogels have also been synthesized directly from their respective LDH precursors. The successful syntheses of MgAl-LDH and NiAl-LDH nanoparticles were confirmed by the characteristic hydrotalcite diffraction peaks in the XRD patterns (Figure 7).[30,31] After thermal treatment, the LDH precursors were completely reduced to their corresponding metal oxide nanoparticles. The MgAl-LDH precursor was converted to the composite of MgO and $MgAl_2O_4$, as indicated by the relevant XRD peaks (Figure 7a),[1] while the reduction of NiAl-LDH resulted in the formation of nickel-metal nanoparticles (Figure 7b).[31] SEM micrographs (Figure 7c,d) showed the good distribution and high uniformity of the mixed metal oxide nanoparticles on the surface of the rGO sheets. This observation was also supported by the homogenous distribution of C, O, Ni, and Al elements in the Ni-Al_2O_3/rGO hybrid aerogel by EDX mapping (Figure S16, ESI).

XPS survey scans corroborated the presence of only C, O, Ni, and Al atoms in the NiAl-LDH powder, Ni-Al_2O_3 powder, and Ni-Al_2O_3/rGO aerogel (Figure S17, ESI). Deconvolution of the XPS high-resolution scan in the C 1s region suggested the presence of C−C, C−O, and C═O functional groups in both NiAl-LDH and Ni-Al_2O_3 powder. For the Ni-Al_2O_3/rGO aerogel, the C═C peak became sharper and a new peak associated with O−C═O binding emerged ascribed to the presence of the rGO sheets (Figure 8a).[32] Peak fittings in the Ni 2p region showed the reductions of Ni^{2+} species present in the NiAl-LDH powder to metallic Ni in the Ni-Al_2O_3 powder and Ni-Al_2O_3/rGO aerogel (Figure 8b).[33] The peaks attributed to the Ni^{2+} oxidation state of the thermally reduced samples were caused by the oxidation of nickel under an air atmosphere. Similarly, the two oxidized aluminum species (i.e., $Al(OH)_3$ and Al_2O_3) in the LDH precursor were completely converted into aluminum oxide under the thermal treatment conditions,[1,14] as seen in the slight shift of the binding energy at around 75 eV, due to charge transfer between the nanocarbon and the metal oxides (Figure 8c). The successful reduction of GO in the NiAl-LDH/GO aerogel to rGO in the

https://doi.org/10.1021/acsami.1c10428
ACS Appl. Mater. Interfaces 2021, 13, 36201−36212

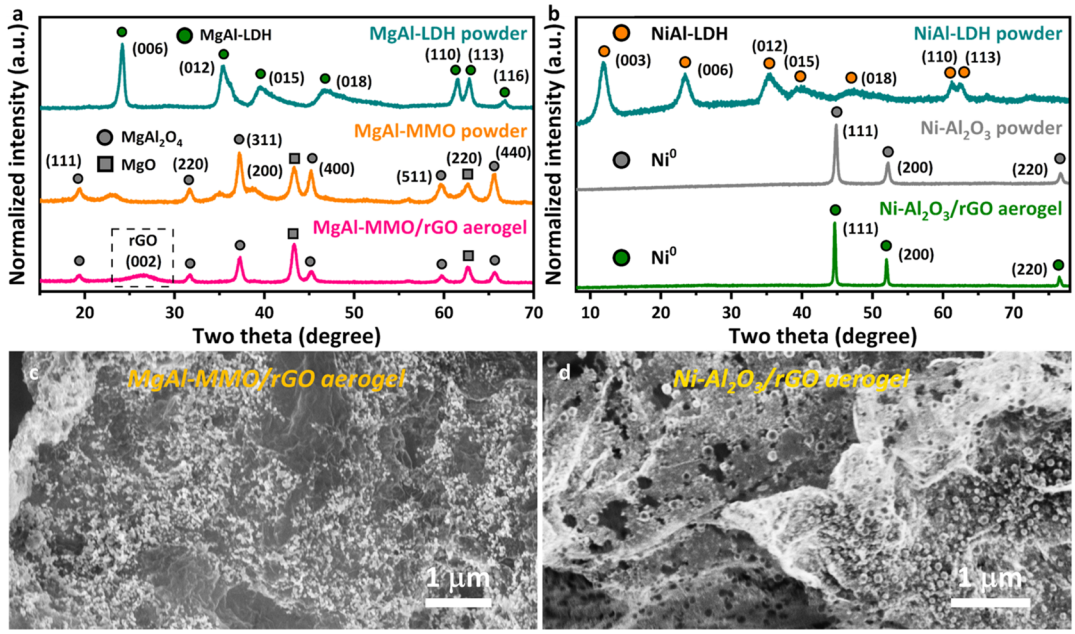

Figure 7. (a) XRD patterns of the MgAl-LDH powder, MgAl-MMO powder, and MgAl-MMO/rGO aerogel. (b) XRD patterns of the NiAl-LDH/GO aerogel and Ni-Al_2O_3/rGO aerogel. SEM micrographs of the MgAl-MMO/rGO aerogel (c) and the Ni-Al_2O_3/rGO aerogel (d).

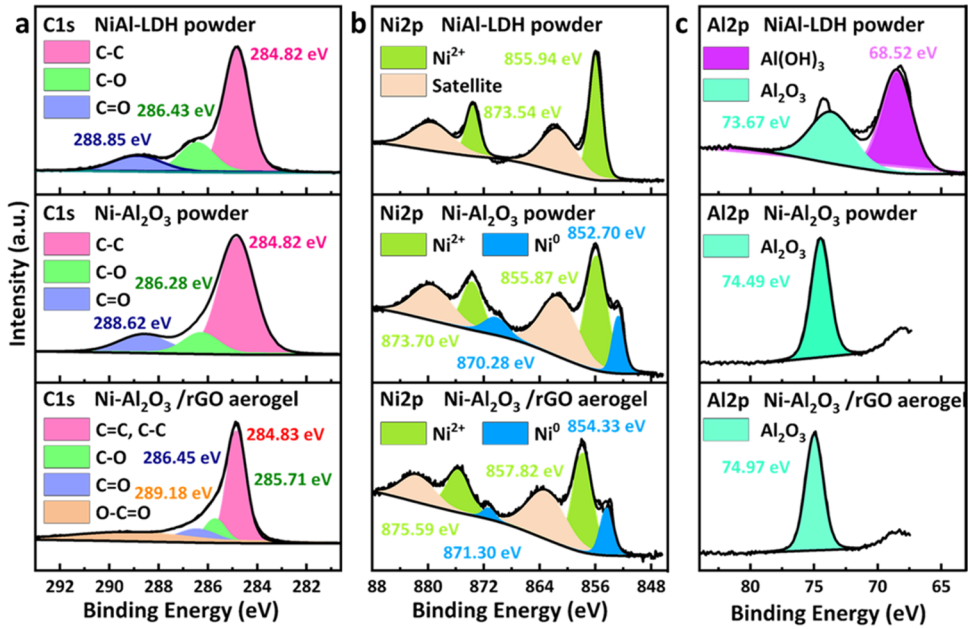

Figure 8. XPS high-resolution scan in the C 1s (a), Ni 2p (b), and Al 2p (c) region of NiAl-LDH powder, Ni-Al_2O_3 powder, and Ni-Al_2O_3/rGO aerogel.

Ni-Al_2O_3/rGO aerogel was confirmed by the increase of the I_D/I_G ratio from 0.96 to 1.32 in the Raman spectra (Figure S18, ESI), consistent with reported Raman results of thermally reduced GO.[1] As expected, both the MgAl-MMO/rGO aerogel and the Ni-Al_2O_3/rGO aerogel exhibited good electric conductivity features, as demonstrated by the stable and linear $I-U$ curves, essential for electrothermal applications (Figure S19, ESI).

Temperature-Swing Joule Heating Simulations. The good electrical conductivity of the rGO support framework was visually demonstrated by the lighting of an LED bulb using a button cell, when connected through the aerogel, as shown in ESI Figure S20. For industrially important temperature-swing adsorption experiments, such as CO_2 sorption using LDH-derived sorbents, the gas is adsorbed onto the solid adsorbents through physisorption (van der Waals force) and chemisorption at an elevated temperature (e.g., 300 °C). To release the gas after reaching equilibrium, a higher temperature (i.e., 400 °C) is required to overcome the forces and the bonding energy between the CO_2 molecules and the adsorbents.[34] For the solid CO_2 adsorbents, a significant amount of cost involved in the carbon capture process originates from the large energy consumption that arises during the recovery of the captured CO_2 (i.e., regeneration of the adsorbents), using traditional energy-demanding, non-uniform external oven heating.[35] However, a new type of adsorbent system, which can embrace

https://doi.org/10.1021/acsami.1c10428
ACS Appl. Mater. Interfaces 2021, 13, 36201−36212

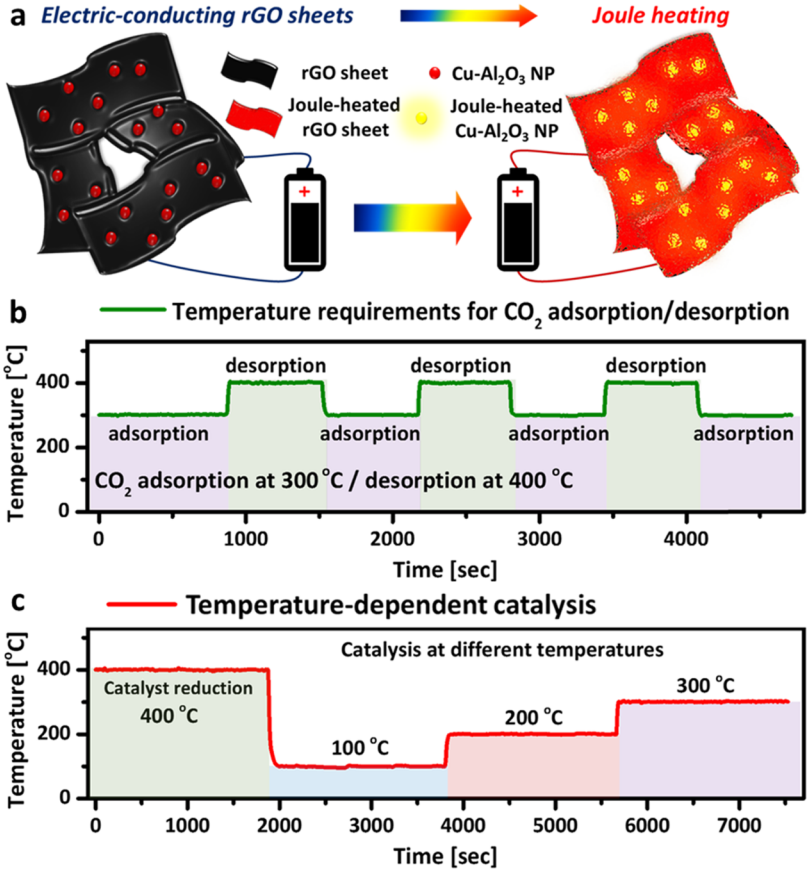

Figure 9. (a) Schematics of internal microstructures of the Cu-Al_2O_3/rGO aerogel under Joule heating. (b, c) Joule heating temperature stability of the Cu-Al_2O_3/rGO aerogel over extended periods at different temperatures relevant to pre-combustion CO_2 adsorption/desorption and catalysis.

the challenging features of high sorption capacity, energy-efficient recovery, selectivity, fast heating/cooling kinetics, and stability under extensive cycling, is highly desirable if one is to satisfy the global demand for CO_2 reduction and the increasing awareness of a circular economy. As electrons are capable of hopping across the well-combined and interconnected rGO sheets, the embedded functional nanoparticles can be heated simultaneously and uniformly in the entire 3D monolithic aerogel (Figure 9a).[36] To simulate the temperature-swing CO_2 adsorption process, the hybrid aerogel was continuously cycled, with the temperature switching between 300 and 400 °C. Because of the extremely fast heating and cooling kinetics, as well as the relative ease of temperature control, the aerogel can be adjusted to desired temperatures almost immediately, maintaining the preset voltage for extended periods (Figure 9b and ESI Figure 21a). For temperature-dependent catalytic processes, such as the water−gas shift reactions and the reverse water−gas shift reactions, catalysts are normally required to undergo thermal reduction at a relatively high temperature to remove impurities, before the experiment.[37,38] For instance, the CuO/Fe_2O_3 catalysts prepared by Zhu et al.[37] for the high-temperature water−gas shift reaction were required to be activated at 350 °C, for 1 h, to remove adsorbed impurities before the catalytic tests. In another reaction, Bahmanpour et al.[38] activated their Cu/Al_2O_3 catalysts at 300 °C for 1 h in the presence of hydrogen, prior to the conduction of the reverse water−gas shift reaction. By introducing the rGO support framework, the hybrid aerogel can be easily switched to different temperatures (e.g., 100−400 °C) while remaining electrically stable and thermally stable for the remainder of the reaction (Figure 9c and ESI Figure 21b).

Figure 10a shows the proportional increment of the aerogel temperature under Joule heating with an increase in the power input. The temperature distribution of the hybrid aerogel at various power inputs was relatively uniform from the center to the edge, albeit significantly dropped at the aerogel/air interface due to strong convective heat dissipation (Figure S22, ESI). Faster heat dissipation at the aerogel/air interface

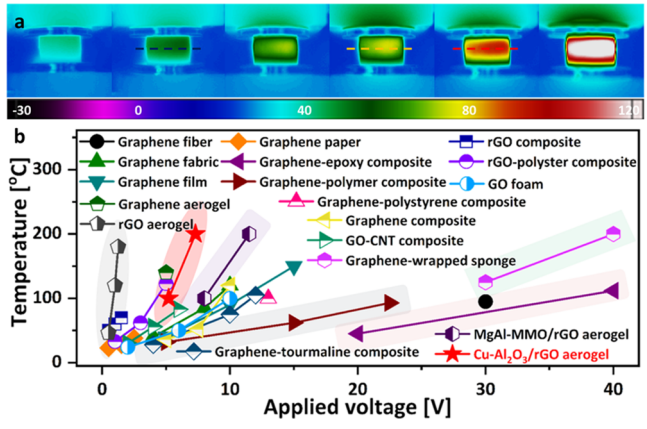

Figure 10. (a) Thermal images of the Cu-Al_2O_3/rGO aerogel under Joule heating. (b) Applied voltage versus Joule-heating temperature of different types of nanocarbon-based materials, as reported in the literature.

https://doi.org/10.1021/acsami.1c10428
ACS Appl. Mater. Interfaces 2021, 13, 36201−36212

was observed at higher Joule heating temperatures. To prevent unnecessary energy loss during the heating process at high temperatures, the aerogel can be covered by insulating materials.[15] Interestingly, compared with the reported carbon-based Joule heating materials (e.g., graphene fibers, graphene fabrics, graphene films, graphene composites, graphene hybrids, and graphene foams),[1,15,39−53] the Cu-Al_2O_3/rGO aerogel exhibited the highest Joule heating temperature at a relatively low applied voltage (Figure 10b), even in the presence of a large number of embedded nanoparticles. The results demonstrate the potential of the as-prepared Cu-Al_2O_3/rGO aerogel to be used as recyclable, highly energy-efficient multifunctional hybrid materials for use in temperature-dependent sorption, catalysis, sensing, etc.

CONCLUSIONS

In summary, 3D-structured rGO aerogels have been exploited as an electrically-heatable support framework for LDH-derived Cu-Al_2O_3 nanoparticles via a facile wet chemical synthetic approach. The hybrid aerogel exhibited a wide spectrum of performance enhancements, including the effective inhibition of aggregation of nanoparticles, enlarged specific surface area, highly aligned macro-channels, and hierarchically porous microstructures. Detailed materials characterization demonstrated the reduction of Cu^{2+} species to metallic copper and transformation of aluminum species to aluminum oxide in the hybrid aerogel after thermal treatment. The introduction of the conductive rGO support framework enables stable and controllable Joule heating of the hybrid aerogel with the prominent characteristics of very high heating rates (up to 636 K/min), high cooling rates (up to 336 K/min), uniform temperature distribution across the structure, and low energy consumption. The syntheses approach employed in this study can be adapted towards the fabrication of other types of nanoparticle/nanocarbon hybrid aerogels (e.g., MgAl-MMO/rGO aerogel and Ni-Al_2O_3/rGO aerogel) with Joule heating capacities for various applications. The temperature-swing Joule heating simulations demonstrated the feasibility and convenience of using the hybrid aerogel for important industrial applications (e.g., CO_2 capture and water−gas shift reaction) under appropriate conditions. Future studies are likely to explore different types of nanocarbons, the impact of nanoparticle loadings, and their influence on the properties of materials. More generally, these findings will provide new functionalities towards widely used functional nanoparticles and broaden the potential application range of nanoparticle/nanocarbon hybrid aerogels, such as heterogeneous catalysis, energy conversion, supercapacitor operation, and sensing.

ASSOCIATED CONTENT

Supporting Information

The Supporting Information is available free of charge at https://pubs.acs.org/doi/10.1021/acsami.1c10428.

Additional experimental details, materials, and methods, including schematics of the experimental setup of the Joule heating measurements. Joule heating parameters of different aerogels. XANES spectra, XPS analyses, SEM micrographs, EDX mapping, Raman spectra, and TGA curve of different materials. Digital images of the aerogels. Bi-exponential function model fitting for the heating/cooling kinetics (PDF)

AUTHOR INFORMATION

Corresponding Authors

Dong Xia − *School of Chemistry, University of Leeds, Leeds LS2 9JT, U.K.*; orcid.org/0000-0001-9302-4789; Email: xiadong0322@qq.com

Heng Li − *Key Laboratory of Estuarine Ecological Security and Environmental Health, Tan Kah Kee College, Xiamen University, 363105 Zhangzhou, China*; Email: liheng310@foxmail.com

Peng Huang − *Department of Materials, University of Manchester, Manchester M13 9PL, U.K.*; Email: peng.huang@manchester.ac.uk

Authors

Jamie Mannering − *School of Chemistry, University of Leeds, Leeds LS2 9JT, U.K.*

Qun Li − *Department of Chemical and Biochemical Engineering, College of Chemistry and Chemical Engineering, Xiamen University, Xiamen 361005, China*

Alexander F. Massey − *School of Chemistry, University of Leeds, Leeds LS2 9JT, U.K.*

Alexander N. Kulak − *School of Chemistry, University of Leeds, Leeds LS2 9JT, U.K.*; orcid.org/0000-0002-2798-9301

Robert Menzel − *School of Chemistry, University of Leeds, Leeds LS2 9JT, U.K.*

Complete contact information is available at: https://pubs.acs.org/10.1021/acsami.1c10428

Notes

The authors declare no competing financial interest.

ACKNOWLEDGMENTS

This research was sponsored by the China Scholarship Council and the University of Leeds. The research of H.L. was supported by the National Key R&D Program of China (2019YFC1805801) and the National Natural Science Foundation of China (22038012). The authors would like to thank Diamond Light Source for providing beamtime for XANES measurements and Dr Yifei Xu for the Raman measurements.

NOMENCLATURE, SYMBOLS, AND ACRONYMS

LDHs, layered double hydroxides
MMO, mixed metal oxides
GO, graphene oxide
PEEK, poly(ether-ether-ketone)
BET, Brunauer−Emmett−Teller
XANES, X-ray absorption near edge structure
SEM, scanning electron microscopy
TEM, transmission electron microscopy
CuAl-LDH, CuAl-layered double hydroxides
Cu-Al_2O_3/rGO aerogel, Cu-Al_2O_3 supported by rGO aerogel
NiAl-LDH/GO aerogel, NiAl-LDH supported by GO aerogel
MgAl-LDH, MgAl-layered double hydroxides
MgAl-LDH/GO aerogel, MgAl-LDH supported by GO aerogel
$d_{spacing}$, lattice spacing (nm)
SSA, specific surface area (m^2/g)
κ, thermal conductivity ($W \cdot m^{-1} \cdot K^{-1}$)

https://doi.org/10.1021/acsami.1c10428
ACS Appl. Mater. Interfaces 2021, 13, 36201−36212

σ_0, electrical conductivity prefactor
T, Joule heating temperature (°C)
E_a, activation energy (eV)
DTG, derivative thermogravimetry
HTs, hydrotalcites
rGO, reduced-graphene-oxide
PVA, poly(vinyl alcohol)
XRD, X-ray diffraction
BJH, Barrett−Joyner−Halenda
XPS, X-ray photoelectron spectroscopy
EDX, energy-dispersive X-ray analysis
TGA, thermogravimetric analysis
CuAl-LDH/GO aerogel, CuAl-LDH supported by GO aerogel
NiAl-LDH, NiAl-layered double hydroxides
Ni-Al_2O_3/rGO aerogel, Ni-Al_2O_3 supported by rGO aerogel
MgAl-MMO, thermally reduced MgAl-LDH
MgAl-MMO/rGO aerogel, MgAl-MMO supported by rGO aerogel
D_p, average crystallite domain size (nm)
σ, electrical conductivity (S/m)
VRH, variable-range hopping
T_0, temperature coefficient
σ_a, pre-exponential factor
k_B, Boltzmann's constant

REFERENCES

(1) Xia, D.; Li, H.; Mannering, J.; Huang, P.; Zheng, X.; Kulak, A.; Baker, D.; Iruretagoyena, D.; Menzel, R. Electrically heatable graphene aerogels as nanoparticle supports in adsorptive desulfurization and high-pressure CO_2 capture. *Adv. Funct. Mater.* **2020**, *30*, No. 2002788.

(2) Meili, L.; Lins, P. V.; Zanta, C.; Soletti, J. I.; Ribeiro, L. M. O.; Dornelas, C. B.; Silva, T. L.; Vieira, M. G. A. MgAl-LDH/Biochar composites for methylene blue removal by adsorption. *Appl. Clay Sci.* **2019**, *168*, 11−20.

(3) Menzel, R.; Iruretagoyena, D.; Wang, Y.; Bawaked, S. M.; Mokhtar, M.; Al-Thabaiti, S. A.; Basahel, S. N.; Shaffer, M. S. P. Graphene oxide/mixed metal oxide hybrid materials for enhanced adsorption desulfurization of liquid hydrocarbon fuels. *Fuel* **2016**, *181*, 531−536.

(4) Yang, Z.Z.; Wei, J. J.; Zeng, G. M.; Zhang, H. Q.; Tan, X. F.; Ma, C.; Li, X. C.; Li, Z. H.; Zhang, C. A review on strategies to LDH-based materials to improve adsorption capacity and photoreduction efficiency for CO_2. *Coordin. Chem. Rev.* **2019**, *386*, 154−182.

(5) Chen, Y.; Zhang, S.; Han, X.; Zhang, X.; Yi, M.; Yang, S.; Yu, D.; Liu, W. Catalytic dechlorination and charring reaction of polyvinyl chloride by CuAl layered double hydroxide. *Energy Fuels* **2018**, *32*, 2407−2413.

(6) Wang, Y.; Dou, L.; Zhang, H. Nanosheet array-like palladium-catalysts Pdx/rGO@CoAl-LDH via lattice atomic-confined in situ reduction for highly efficient Heck coupling reaction. *ACS Appl. Mater. Interfaces* **2017**, *9*, 38784−38795.

(7) Li, L.; San Hui, K.; Hui, K. N.; Xia, Q.; Fu, J.; Cho, Y. R. Facile synthesis of NiAl layered double hydroxide nanoplates for high-performance asymmetric supercapacitor. *J. Alloys Compd.* **2017**, *721*, 803−812.

(8) Guo, Y.; Hong, X.; Wang, Y.; Li, Q.; Meng, J.; Dai, R.; Liu, X.; He, L.; Mai, L. Multicomponent hierarchical Cu-doped NiCo-LDH/CuO double arrays for ultralong-life hybrid fiber supercapacitor. *Adv. Funct. Mater.* **2019**, *29*, No. 1809004.

(9) Liu, J.; Wang, J.; Zhang, B.; Ruan, Y.; Lv, L.; Ji, X.; Xu, K.; Miao, L.; Jiang, J. Hierarchical $NiCo_2S_4$@NiFe LDH heterostructures supported on nickel foam for enhanced overall-water-splitting activity. *ACS Appl. Mater. Interfaces* **2017**, *9*, 15364−15372.

(10) Arif, M.; Yasin, G.; Shakeel, M.; Fang, X.; Gao, R.; Ji, S.; Yan, D. Coupling of bifunctional CoMn-layered double hydroxide@graphitic C_3N_4 nanohybrids towards efficient photoelectrochemical overall water splitting. *Chem-Asian J.* **2018**, *13*, 1045−1052.

(11) Chetty, T.; Dasireddy, V. D. B. C.; Callanan, L. H.; Friedrich, H. B. Continuous flow preferential hydrogenation of an octanal/octene mixture using Cu/Al_2O_3 catalysts. *ACS Omega* **2018**, *3*, 7911−7924.

(12) Zaccheria, F.; Ravasio, N.; Psaro, R.; Fusi, A. Synthetic scope of alcohol transfer dehydrogenation catalyzed by Cu/Al_2O_3: A new metallic catalyst with unusual selectivity. *Chem.-Eur. J.* **2006**, *12*, 6426.

(13) Park, S.; Kannapu, H. P. R.; Jeong, C.; Kim, J.; Suh, Y. W. Highly active mesoporous Cu-Al_2O_3 catalyst for the hydrodeoxygenation of furfural to 2-methylfuran. *ChemCatChem* **2020**, *12*, 105−111.

(14) Xia, D.; Huang, P.; Li, H.; Rubio Carrero, N. Fast and efficient electrical-thermal responses of functional nanoparticle decorated nanocarbon aerogels. *Chem. Commun.* **2020**, *56*, 14393−14396.

(15) Menzel, R.; Barg, S.; Miranda, M.; Anthony, D. B.; Bawaked, S. M.; Mokhtar, M.; Al-Thabaiti, S. A.; Basahel, S. N.; Saiz, E.; Shaffer, M. S. P. Joule heating characteristics of emulsion-templated graphene aerogels. *Adv. Funct. Mater.* **2015**, *25*, 28−35.

(16) Li, J.; Zhang, S.; Chen, Y.; Liu, T.; Liu, C.; Zhang, X.; Yi, M.; Chu, Z.; Han, X. A novel three-dimensional hierarchical CuAl layered double hydroxide with excellent catalytic activity for degradation of methyl orange. *RSC Adv.* **2017**, *7*, 29051−29057.

(17) Ahsan, M. A.; Jabbari, V.; El-Gendy, A. A.; Curry, M. L.; Noveron, J. C. Ultrafast catalytic reduction of environmental pollutants in water via MOF-derived magnetic Ni and Cu nanoparticles encapsulated in porous carbon. *Appl. Surf. Sci.* **2019**, *497*, No. 143608.

(18) Zhao, H. B.; Cheng, J. B.; Zhu, J. Y.; Wang, Y. Z. Ultralight CoNi/rGO aerogels toward excellent microwave absorption at ultrathin thickness. *J. Mater. Chem. C* **2019**, *7*, 441−448.

(19) Jung, H.; Lee, S. Y.; Lee, C. W.; Cho, M. K.; Won, D. H.; Kim, C.; Oh, H. S.; Min, B. K.; Hwang, Y. J. Electrochemical fragmentation of Cu_2O nanoparticles enhancing selective C-C coupling from CO_2 reduction reaction. *J. Am. Chem. Soc.* **2019**, *141*, 4624−4633.

(20) Liu, M.; Zhang, P.; Qu, Z.; Yan, Y.; Lai, C.; Liu, T.; Zhang, S. Conductive carbon nanofiber interpenetrated graphene architecture for ultra-stable sodium ion battery. *Nat. Commun.* **2019**, *10*, No. 3917.

(21) Liu, M.; Li, B.; Zhou, H.; Chen, C.; Liu, Y.; Liu, T. Extraordinary rate capability achieved by a 3D "skeleton/skin" carbon aerogel-polyaniline hybrid with vertically aligned pores. *Chem. Commun.* **2017**, *53*, 2810−2813.

(22) Wang, C.; Chen, X.; Wang, B.; Huang, M.; Wang, B.; Jiang, Y.; Ruoff, R. S. Freeze-casting produces a graphene oxide aerogel with a radial and centrosymmetric structure. *ACS Nano* **2018**, *12*, 5816−5825.

(23) Yan, Y.; Zhang, P.; Qu, Z.; Tong, M.; Zhao, S.; Li, Z.; Liu, M.; Lin, Z. Carbon/sulfur aerogel with adequate mesoporous channels as robust polysulfide confinement matrix for highly stable lithium-sulfur battery. *Nano Lett.* **2020**, *20*, 7662−7669.

(24) Barg, S.; Perez, F. M.; Ni, N.; do Vale Pereira, P.; Maher, R. C.; Garcia-Tuñon, E.; Eslava, S.; Agnoli, S.; Mattevi, C.; Saiz, E. Mesoscale assembly of chemically modified graphene into complex cellular networks. *Nat. Commun.* **2014**, *5*, No. 4328.

(25) Cepellotti, A.; Fugallo, G.; Paulatto, L.; Lazzeri, M.; Mauri, F.; Marzari, N. Phonon hydrodynamics in two-dimensional materials. *Nat. Commun.* **2015**, *6*, No. 6400.

(26) Li, T.; Pickel, A. D.; Yao, Y.; Chen, Y.; Zeng, Y.; Lacey, S. D.; Li, Y.; Wang, Y.; Dai, J.; Wang, Y.; et al. Thermoelectric properties and performance of flexible reduced graphene oxide films up to 3,000 K. *Nat. Energy* **2018**, *3*, 148−156.

(27) Jiang, X.; Xu, C.; Gao, T.; Bando, Y.; Golberg, D.; Dai, P.; Hu, M.; Ma, R.; Hu, Z.; Wang, X. B. Flexible conductive polymer composite materials based on strutted graphene foam. *Compos. Commun.* **2021**, *25*, No. 100757.

https://doi.org/10.1021/acsami.1c10428
ACS Appl. Mater. Interfaces 2021, 13, 36201−36212

(28) Qi, X.-d.; Wang, W. Y.; Xiao, Y. J.; Huang, T.; Zhang, N.; Yang, J. H.; Wang, Y. Tailoring the hybrid network structure of boron nitride/carbon nanotube to achieve thermally conductive poly(vinylidene fluoride) composites. *Compos. Commun.* **2019**, *13*, 30−36.
(29) Li, H.; Fu, C.; Chen, N.; Zhang, T.; Liu, J.; Du, G.; Ren, L.; Zeng, X.; Sun, R. Ice-templated assembly strategy to construct three-dimensional thermally conductive networks of BN nanosheets and silver nanowires in polymer composites. *Compos. Commun.* **2021**, *25*, No. 100601.
(30) Huang, Q.; Chen, Y.; Yu, H.; Yan, L.; Zhang, J.; Wang, B.; Du, B.; Xing, L. Magnetic graphene oxide/MgAl-layered double hydroxide nanocomposite: one-pot solvothermal synthesis, adsorption performance and mechanisms for Pb^{2+}, Cd^{2+}, and Cu^{2+}. *Chem. Eng. J.* **2018**, *341*, 1−9.
(31) Chen, H.; He, S.; Xu, M.; Wei, M.; Evans, D. G.; Duan, X. Promoted synergic catalysis between metal Ni and acid-base sites toward oxidant-free dehydrogenation of alcohols. *ACS Catal.* **2017**, *7*, 2735−2743.
(32) Wei, Z.; Li, Y.; Dou, L.; Ahmad, M.; Zhang, H. $Cu_{3-x}Ni_xAl$-layered double hydroxide-reduced graphene oxide nanosheet array for the reduction of 4-nitrophenol. *ACS Appl. Nano Mater.* **2019**, *2*, 2383−2396.
(33) Sun, C.; Beaunier, P.; Da Costa, P. Effect of ceria promotion on the catalytic performance of Ni/SBA-16 catalysts for CO_2 methanation. *Catal. Sci. Technol.* **2020**, *10*, 6330−6341.
(34) De Marco, M.; Menzel, R.; Bawaked, S. M.; Mokhtar, M.; Obaid, A. Y.; Basahel, S. N.; Shaffer, M. S. P. Hybrid effects in graphene oxide/carbon nanotube-supported layered double hydroxides: enhancing the CO_2 sorption properties. *Carbon* **2017**, *123*, 616−627.
(35) Choi, W.; Min, K.; Kim, C.; Ko, Y. S.; Jeon, J. W.; Seo, H.; Park, Y.-K.; Choi, M. Epoxide-functionalization of polyethyleneimine for synthesis of stable carbon dioxide adsorbent in temperature swing adsorption. *Nat. Commun.* **2016**, *7*, No. 12640.
(36) Lillia, S.; Bonalumi, D.; Grande, C.; Manzolini, G. A comprehensive modeling of the hybrid temperature electric swing adsorption process for CO_2 capture. *Int. J. Greenhouse Gas Control* **2018**, *74*, 155−173.
(37) Zhu, M.; Tian, P.; Kurtz, R.; Lunkenbein, T.; Xu, J.; Schlögl, R.; Wachs, I. E.; Han, Y. F. Strong metal-support interactions between copper and iron oxide during the high-temperature water-gas shift reaction. *Angew. Chem. Int. Ed.* **2019**, *58*, 9083−9087.
(38) Bahmanpour, A. M.; Héroguel, F.; Kılıç, M.; Baranowski, C. J.; Artiglia, L.; Röthlisberger, U.; Luterbacher, J. S.; Kröcher, O. Cu-Al spinel as a highly active and stable catalyst for the reverse water gas shift reaction. *ACS Catal.* **2019**, *9*, 6243−6251.
(39) Noh, S. H.; Eom, W.; Lee, W. J.; Park, H.; Ambade, S. B.; Kim, S. O.; Han, T. H. Joule heating-induced sp2-restoration in graphene fibers. *Carbon* **2019**, *142*, 230−237.
(40) Tian, M.; Hao, Y.; Qu, L.; Zhu, S.; Zhang, X.; Chen, S. Enhanced electrothermal efficiency of flexible graphene fabric Joule heaters with the aid of graphene oxide. *Mater. Lett.* **2019**, *234*, 101−104.
(41) Ding, G.; Jiao, W.; Wang, R.; Niu, Y.; Hao, L.; Yang, F.; Liu, W. A biomimetic, multifunctional, superhydrophobic graphene film with self-sensing and fast recovery properties for microdroplet transportation. *J. Mater. Chem. A* **2017**, *5*, 17325−17334.
(42) Guo, Y.; Dun, C.; Xu, J.; Mu, J.; Li, P.; Gu, L.; Hou, C.; Hewitt, C. A.; Zhang, Q.; Li, Y.; et al. Ultrathin, washable, and large-area graphene papers for personal thermal management. *Small* **2017**, *13*, No. 1702645.
(43) Raji, A.-R. O.; Varadhachary, T.; Nan, K.; Wang, T.; Lin, J.; Ji, Y.; Genorio, B.; Zhu, Y.; Kittrell, C.; Tour, J. M. Composites of graphene nanoribbon stacks and epoxy for joule heating and deicing of surfaces. *ACS Appl. Mater. Interfaces* **2016**, *8*, 3551−3556.
(44) Zhang, D.; Xu, S.; Zhao, X.; Qian, W.; Bowen, C. R.; Yang, Y. Wireless monitoring of small strains in intelligent robots via a Joule heating effect in stretchable graphene-polymer nanocomposites. *Adv. Funct. Mater.* **2020**, *30*, No. 1910809.
(45) Hazarika, A.; Deka, B. K.; Kim, D.; Jeong, H. E.; Park, Y. B.; Park, H. W. Woven kevlar fiber/polydimethylsiloxane/reduced graphene oxide composite-based personal thermal management with freestanding Cu-Ni core-shell nanowires. *Nano Lett.* **2018**, *18*, 6731−6739.
(46) Hazarika, A.; Deka, B. K.; Kim, D.; Roh, H. D.; Park, Y.-B.; Park, H. W. Fabrication and synthesis of highly ordered nickel cobalt sulfide nanowire-grown woven kevlar fiber/reduced graphene oxide/polyester composites. *ACS Appl. Mater. Interfaces* **2017**, *9*, 36311−36319.
(47) Bento, J. L.; Brown, E.; Woltornist, S. J.; Adamson, D. H. Thermal and electrical properties of nanocomposites based on self-assembled pristine graphene. *Adv. Funct. Mater.* **2017**, *27*, No. 1604277.
(48) Hao, Y.; Tian, M.; Zhao, H.; Qu, L.; Zhu, S.; Zhang, X.; Chen, S.; Wang, K.; Ran, J. High efficiency electrothermal graphene/tourmaline composite fabric joule heater with durable abrasion resistance via a spray coating route. *Ind. Eng. Chem. Res.* **2018**, *57*, 13437−13448.
(49) Karim, N.; Zhang, M.; Afroj, S.; Koncherry, V.; Potluri, P.; Novoselov, K. S. Graphene-based surface heater for de-icing applications. *RSC Adv.* **2018**, *8*, 16815−16823.
(50) Zheng, Z.; Jin, J.; Xu, G.-K.; Zou, J.; Wais, U.; Beckett, A.; Heil, T.; Higgins, S.; Guan, L.; Wang, Y.; et al. Highly stable and conductive microcapsules for enhancement of joule heating performance. *ACS Nano* **2016**, *10*, 4695−4703.
(51) Ge, J.; Shi, L. A.; Wang, Y. C.; Zhao, H. Y.; Yao, H. B.; Zhu, Y. B.; Zhang, Y.; Zhu, H. W.; Wu, H. A.; Yu, S. H. Joule-heated graphene-wrapped sponge enables fast clean-up of viscous crude-oil spill. *Nat. Nanotechnol.* **2017**, *12*, 434−440.
(52) D'Elia, E.; Ahmed, H. S.; Feilden, E.; Saiz, E. Electrically-responsive graphene-based shape-memory composites. *Appl. Mater. Today* **2019**, *15*, 185−191.
(53) Liu, Y.; Shi, Q.; Hou, C.; Zhang, Q.; Li, Y.; Wang, H. Versatile mechanically strong and highly conductive chemically converted graphene aerogels. *Carbon* **2017**, *125*, 352−359.

https://doi.org/10.1021/acsami.1c10428
ACS Appl. Mater. Interfaces 2021, 13, 36201−36212